Humidity Dependence of AE Activity in Sheared Quartz Gouges and its Implication for the Micromechanics of Friction

Yasuo Yabe[1]

[1]Research Center for Prediction of Earthquakes and Volcanic Eruptions, Graduate School of Science, Tohoku University

Corresponding author: Yasuo Yabe (yasuo.yabe.e2@tohoku.ac.jp)

Key Points (140 chars):

- When quartz gouges were sheared under higher humidity, AE activity became lower and rate-weakening behavior of friction was enhanced.
- Humidity controls the trade-off between the macroscopic instability and microscopic brittleness of a quartz gouge layer.
- The direct effect of friction and rate dependence of the AE rate are sensitive to the water film coverage on the gouge particle surface.

Key words:

Acoustic emission

Humidity dependence

Pressure solution

Contact junction failure

Trade-off between brittle and plastic deformations

Rotary shear test

Abstract (150 words)

The humidity-dependent acoustic emission (AE) activity in a quartz gouge layer was investigated via sliding-rate step tests. Because AE events are generated by the brittle failure of the contact junction, their activity reflects the micromechanics of friction. AE activity was evaluated by the *m*-value (characterizing amplitude distribution), AE rate (number of events per unit sliding distance), and their sliding-rate dependences. The *m*-value decreased with increasing humidity, suggesting contact junction growth by the pressure solution. Increased humidity decreased the AE rate and enhanced the rate-weakening of friction, implying the role of water in suppressing the brittleness of contact junction and strengthening macroscopic instability. Notably, the relationship between the direct effect of friction and the sliding-rate dependence of AE rate under dry conditions was distinct from those under other conditions, suggesting these are sensitivity to areal fraction of the water film on the surface of the gouge particle.

Plain Language Summary

Water-assisted deformation is known as the micromechanics of the time-dependent healing of rock friction. However, the mechanism by which the healed contacts break during sliding is not well understood. Brittle failure of the contact junctions causes acoustic emissions (AEs). AE activity reflects the brittleness of microscopic deformation. This study examined the humidity dependence of AE activity in a quartz gouge layer during shearing. AE activity was evaluated using the *m*-value, which characterizes the average magnitude, and the AE rate, which is the number of AEs per 1-mm sliding. The *m*-value decreases with increasing water vapor content, whereas it increases under wet conditions, implying that the plastic deformation of the contact junction was implemented by the pressure solution. With increasing humidity, the AE rate decreased, and the rate-weakening behavior of friction was enhanced. The sliding-rate dependence of the AE rate and the direct effect of friction under dry conditions were more significant than those under higher humidity. This implies that these parameters are sensitive to the areal fraction of the water film on the gouge particle surface. This study demonstrated the ability of AE monitoring to investigate the micromechanics of friction.

1 Introduction

The majority of the slip on a natural fault is accommodated in a narrow zone called the fault core (Chester et al. 2012). Because the fault core is filled with fine-grained fractured rocks, knowledge of the frictional properties of granular rocks, such as quartz sand, is important for understanding various fault behaviors, from stable creep to earthquakes. Many studies have been conducted to elucidate the frictional behavior of granular rocks and their underlying processes in natural faults (Chester et al., 2012; Mngadi et al., 2021; Moore et al., 2009), laboratories (Bedford & Faulkner, 2021; Mair et al., 2002; Marone et al., 1992; Marone & Scholz, 1989), and numerical models (Casas et al., 2023; Johnson et al., 2021). Considerable efforts have focused on elucidating the microscopic physicochemical processes involved in the healing of contact junctions. Breaking the contact junction is a necessary occurrence during frictional sliding. However, the failure processes of contact junctions are not well understood.

Because acoustic emissions (AEs) are generated by brittle failure in the sheared gouge layer, their activity is expected to reflect the microscopic deformation processes and stress states in the gouge layer. Therefore, AE activity has been analyzed to probe underlying processes of

frictional sliding (Bolton et al., 2022; Gao et al., 2019; Ostapchuk et al., 2021) and preparation processes of stick-slip events (Bolton et al., 2020, 2021; Johnson et al., 2013; Rouet-Leduc et al., 2018). This study investigated AE activity during sliding-rate step tests of a quartz gouge layer under various humidities. The frictional response against the sliding-rate step was evaluated using the rate- and state-dependent friction (RSF) laws (Dieterich, 1979; Ruina 1983). The failure process of the contact junction during frictional sliding is discussed by comparing the humidity dependences of the AE activity and RSF parameters.

2 Experimental Methods

2.1 Sample preparation

A layer of quartz powder (gouge) was sheared using a rotary shear apparatus (Figure 1) to measure its frictional behavior against the sliding-rate steps and AE activity in the gouge layer. The gouge was prepared by grinding quartz sand (>98% of SiO_2), passed through a sieve with 106 μm openings, and stored under a dry condition with a relative humidity (RH) of ~5%. A Teflon ring and plug were attached to the lower forcing block (Figure 1c). The gouge (1.0 g) was spread over the annular interface (outer and inner diameters of 30 and 20 mm, respectively) under ambient conditions. An upper forcing block and a chamber were installed (Figure 1b). Once parallelism between the interfaces of the upper and lower forcing blocks was confirmed, the assembled forcing blocks were set in the rotary shear apparatus, and pre-conditioned air flowed into the chamber for ~17 h to achieve desired humidity conditions. Under dry conditions, air was dehydrated to ~5% RH using silica gel and an anhydrous calcium sulfate desiccant. Under humid conditions (100% RH), air was blown into deionized water before flowing into the chamber. Under wet conditions, ~0.25 g of deionized water was added to the gouge layer before installing the upper forcing block. The assembled forcing blocks were left under humid conditions for ~17 h to allow water to uniformly percolate through the gouge. Pore pressure was not controlled during the tests. Experimental conditions are summarized in Table S1 in Supporting Information S1.

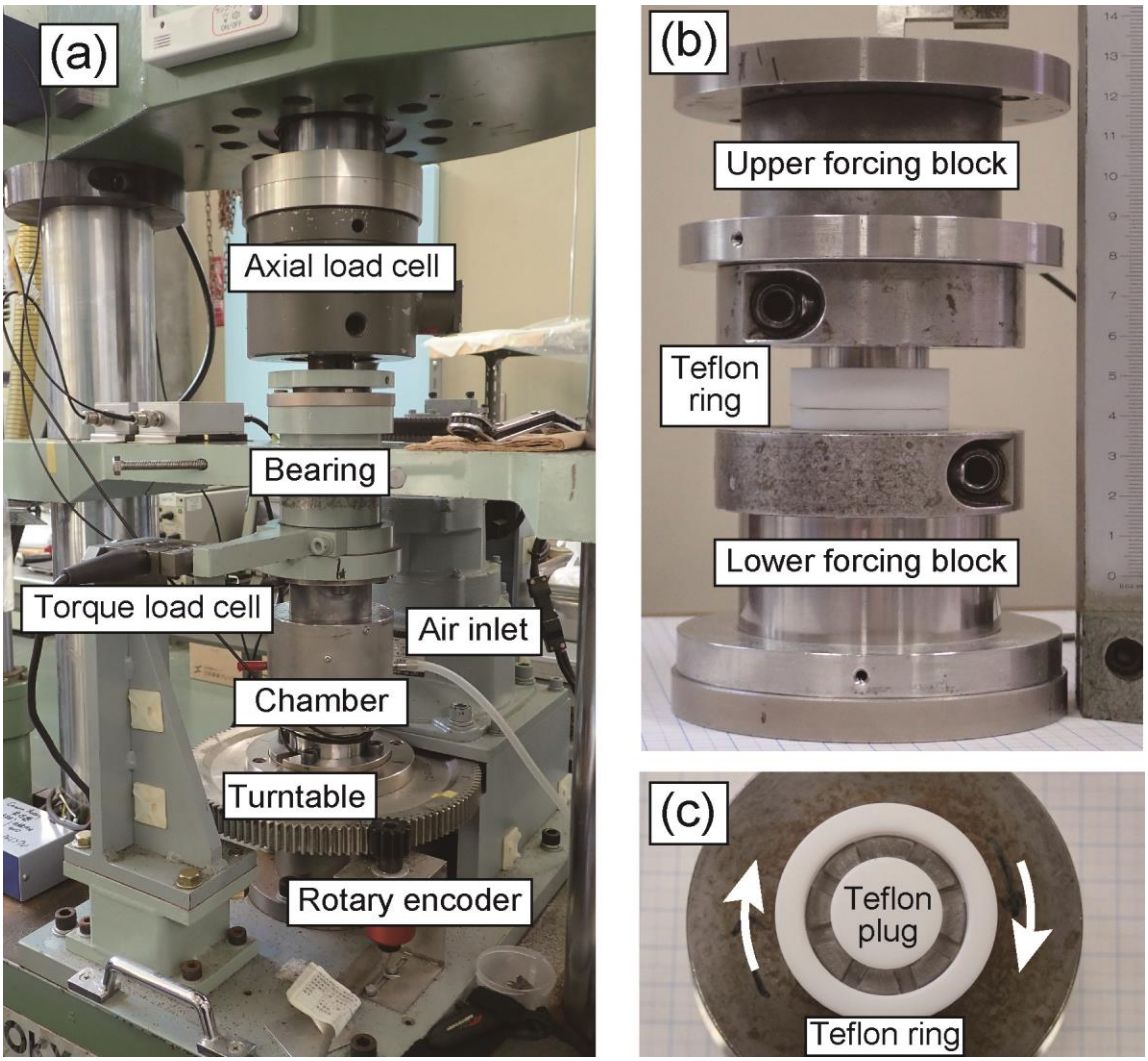

Figure 1. Photos of (**a**) rotary shear apparatus, (**b**) sample assembly without chamber, and (**c**) annular interface confined by Teflon ring and plug. The white arrows in (c) indicate the rotation direction.

97

2.2 Experimental procedures

A normal load applied to the interface was kept constant with an accuracy of ±1.6% or better using a PC-based servo-controlled hydraulic apparatus. Torque was measured 150 mm from the central axis of the upper forcing block. The sliding distance was measured using a rotary encoder attached to a turntable with the lower forcing block. The rotary encoder generated 810,000 pulses per rotation. The normal load and torque were recorded at 10 kHz with 24-bit resolution and resampled by averaging their data for every ~0.1-μm sliding (resolution of the rotary encoder). The normal stress σ_n was calculated by dividing the normal load by the nominal area of the annular interface. When shear stress τ is uniform over the annular interface, it equilibrates with the torque T as $T = 2\pi\tau \int_{r_i}^{r_o} r^2 dr$, where r_o and r_i are the outer and inner radii of the annular interface, respectively.

The gouge was compacted for 1 h at $\sigma_n = 5$ MPa. Then, sliding-rate steps of 4.64-10-21.5-46.4 or 3-10-30-100 μm/s were imposed every 1-mm sliding in the first half of each test. The interval of the sliding-rate step was increased to 2 mm in the second half of each test (Figure 2b), because the AE rate decreased with increasing sliding distance.

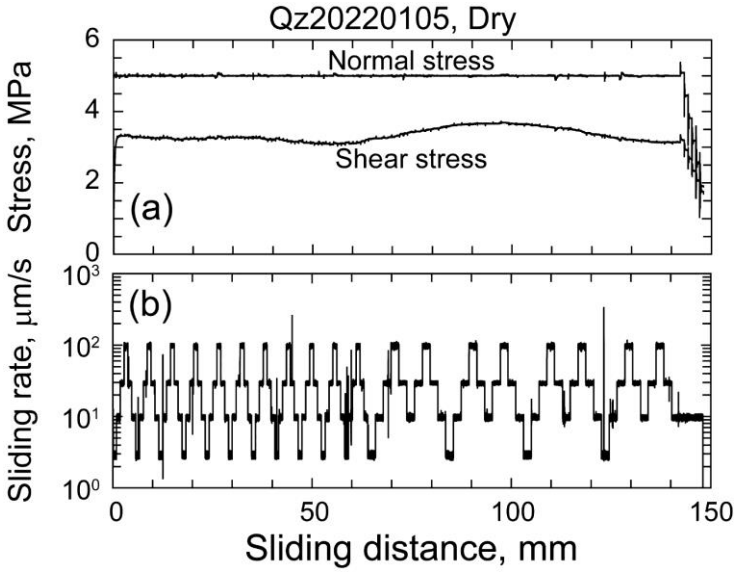

Figure 2. Example of loading history ((**a**) the normal and shear stresses, (**b**) the sliding rate) with respect to the sliding distance for a dry test.

2.3 Acoustic estimation observations and analysis

A broadband (0.5–1.2 MHz), P-wave type AE sensor was installed in the upper and lower forcing blocks to observe AE activity. The outputs of the AE sensor were amplified by 50 or 60 dB, rectified to obtain the AE envelope, and recorded at 100 kHz with 18-bit resolution. After correcting the amplifier gains to unity (0 dB), the AE events were detected as peaks with amplitudes larger than the threshold from the AE envelopes between 5 and 95% of the sliding distance between consecutive sliding-rate steps. As the largest noise level among tests was ~100 μV, the threshold was set to 158 μV. To compare the AE activities at different sliding rates, the AE rate N was defined as the number of AE events per unit sliding distance (1 mm). If the number of detected events is small, the AE rate cannot be evaluated correctly. The AE rates were evaluated only when more than four events were detected. The m-value of Ishimoto-Iida relationship (Ishimoto & Iida, 1939) which characterizes the amplitude distribution of AE events, was estimated using the most likelihood method. The m-value is related to b-value of the Gutenberg-Richter relationship, $m = b + 1$ (Asada et al., 1951).

140

141 2.4 Friction data processing

142 The friction coefficient was calculated by dividing shear stress by normal stress. Because
143 the shear stress was superimposed by a fluctuation with a period of ~80 mm probably due to
144 eccentricity between the upper and lower forcing blocks (Figure 2a), friction coefficient μ_i at
145 sliding distance $d = 0$ mm was estimated by fitting the following function to the friction data for
146 $5 \leq d \leq 120$ mm.

147

$$\mu = \mu_i + \mu_h d + \mu_f \sin\left(2\pi\left(d - d_f\right)/d_r\right) \tag{1}$$

148

149 where μ_h is the hardening rate, and μ_f and d_f are amplitude and initial phase, respectively, of the
150 fluctuation. The period d_r was fixed at 81.56 mm (the sliding distance for one rotation).

151 A theoretical frictional response was calculated by numerically integrating the rate- and
152 state-dependent friction (RSF) laws (Dieterich, 1979; Ruina 1983) with two state variables
153 (Equations 2 and 3) coupled with a quasi-static 1-D spring-slider model (Equation 4) using the
154 fourth order Runge-Kutta method.

155

$$\begin{cases} \mu = \mu_0 + a \ln\left(\dfrac{V}{V_0}\right) + b_1 \ln\left(\dfrac{V_0\theta_1}{Dc_1}\right) + b_2 \ln\left(\dfrac{V_0\theta_2}{Dc_2}\right) & (2) \\ \dfrac{d\theta_i}{dt} = -\dfrac{V\theta_i}{Dc_i} \ln\left(\dfrac{V\theta_i}{Dc_i}\right) & (3) \end{cases}$$

156

157 where t is time. μ and V are friction coefficient and sliding rate, respectively, and μ_0 and V_0 are
158 their reference values. a, b_i and Dc_i ($i = 1, 2$; $Dc_2 > Dc_1$) represent the direct effect, evolution
159 effect, and critical slip distances, respectively. θ_i is state variable, which evolves over Dc_i.

160

$$k\,(V_l - V) - \frac{d\mu}{dt} - \eta\frac{dV}{dt} = 0 \tag{4}$$

161

162 where k is the stiffness of the loading system, and V_l is the loading rate. η represents the seismic
163 radiation damping (Rice, 1993) and was set to 10^{-6} s/μm. The stiffness was determined for each
164 sliding-rate step to reproduce the delay in peak friction after the stepwise change in the sliding
165 rate. The sliding rate measured by the rotary encoder was substituted with V_l.

166 The theoretical frictional response against each sliding-rate step was visually fitted to the
167 observed response. Higher-order friction perturbations were corrected by removing the linear
168 trend estimated from the friction data immediately before each sliding-rate step. The fitting
169 window length was adjusted for each sliding-rate step, such that steady-state sliding after the

sliding-rate step was included. Typical window lengths before and after a step were 50–150 and 150–300 μm, respectively.

3 Results

For $d < 30$ mm, the rate dependence of friction $(a - b)$ and the m-value evolved with sliding (Figures S1-S8 in Supporting Information S1). For these sliding distances, the AE rate decreased steeply. Therefore, averages of parameters of RSF law and AE activity for $50 \leq d \leq 100$ mm were plotted in Figures 3 and 4, respectively, with respect to humidity. The error bars indicate the standard deviation of each parameter for the sliding distance range. Even when the relative humidity was the same, the amount of water vapor differed at different temperatures. Therefore, humidity was represented by the partial water vapor pressure P_v, which was calculated from the air temperature and relative humidity during the test using Tetens's formula (Tetens, 1930) under the assumption that the atmospheric pressure was 1013 hPa. The partial water vapor pressure under wet conditions was set to 1013 hPa.

3.1 Humidity dependences of friction parameters

The friction coefficients were 0.62–0.73 and effect of P_v was insignificant (Figure 3a). The direct effect a was 0.0074 based on the average of the two dry tests. It decreases to 0.0052 at room conditions and slightly increases with P_v to 0.0062 and 0.0064 under humid and wet conditions, respectively (Figure 3b). The evolution effect b_1 increased monotonically with P_v from 0.0034 under dry conditions to 0.0071 under wet conditions (Figure 3c). In contrast, b_2 is 0.0055 under dry conditions and reaches a minimum value of 0.0043 at room conditions (Figure 3d). Subsequently, it increased to 0.0058 and 0.0081 under humid and wet conditions, respectively. As P_v dependences of a and b_2 were similar, they canceled out, and the rate dependence of friction $(a - b;\ b = b_1 + b_2)$ linearly decreased from -0.0015 under dry conditions to -0.0087 under wet conditions with increasing logarithm of P_v (Figure 3f). The critical slip distances Dc_1 and Dc_2 were 3.3 and 30.2 μm under dry conditions, respectively, and took respective minimums of 2.3 and 19.9 μm at room conditions (Figure 3e). Thereafter, Dc_1 increased to 3.1 and 4.6 μm at humid and wet conditions, respectively, with increasing P_v. On the other

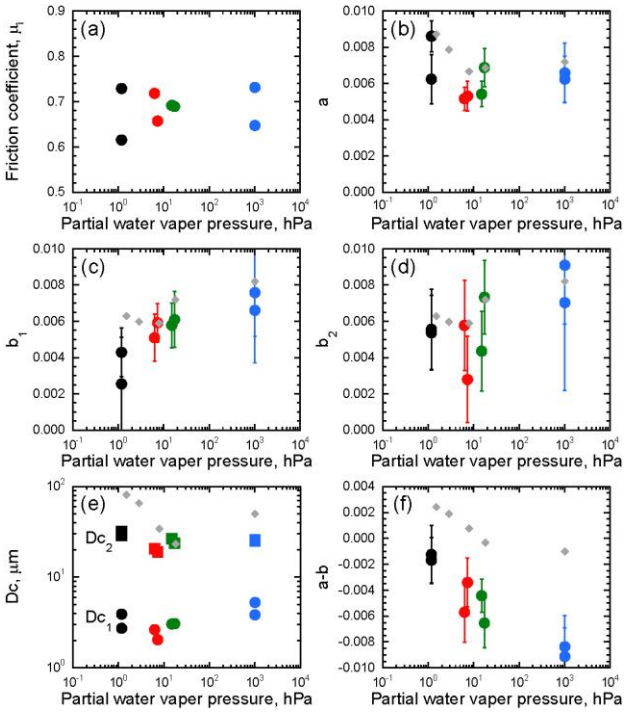

Figure 3. Humidity (P_v) dependences of **(a)** initial friction coefficient μ_i, **(b)** direct effect (a of RFS law), **(c)** evolution effect b_1, **(d)** evolution effect b_2, (**e**) critical slip distances (the circles and squares represent Dc_1 and Dc_2, respectively), and **(f)** sliding-rate dependence of friction $a - b$; $b = b_1 + b_2$). The black, red, green, and blue symbols represent dry, room, humid, and wet conditions, respectively. The small gray diamonds in (b)-(f) are data from Frye & Marone (2002).

hand, Dc_2 took a constant value of 25.3 μm for humid and wet conditions.

3.2 Humidity dependences of AE activity

As AE rate depends on sliding rate in the form of $N \propto V^{\alpha}$, where α is a constant (Yabe, 2002), AE rate at $V = 10$ μm/s was plotted in Figure 4a. It linearly decreased from ~6900 events/mm under dry conditions to ~990 events/mm under wet conditions with increasing P_v in this log-log plot. The sliding-rate dependence of AE rate α was 0.29 at dry conditions and 0.15 for the other conditions (Figure 4b). The *m*-value decreased from 2.10 to 2.04 with increasing P_v from dry to humid conditions (Figure 4c). The higher *m*-value of 2.23 under wet conditions may be due to the presence of liquid water. Sliding-rate dependence of *m*-value was not significant ($dm/d\ln V \approx 0$) regardless of P_v (Figure 4d).

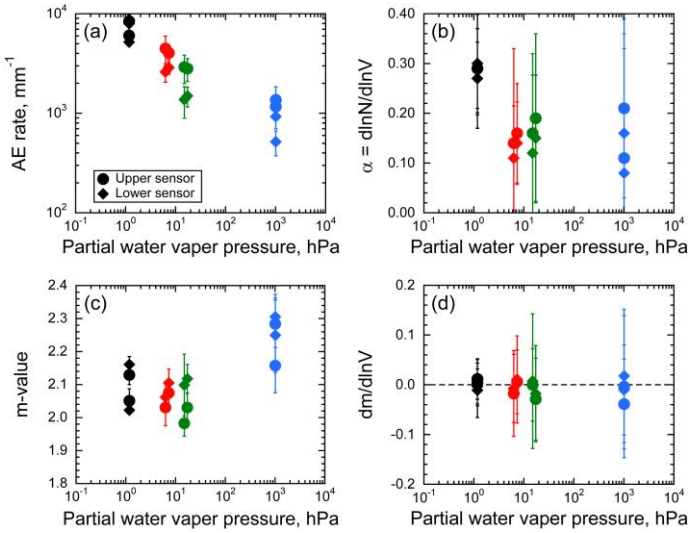

Figure 4. Effects of humidity on **(a)** AE rate at $V = 10$ μm/s, **(b)** sliding-rate dependence of AE rate ($\alpha = d\ln N/d\ln V$). **(c)** the *m*-value and **(d)** sliding-rate dependence of *m*-value. The black, red, green, and blue symbols represent dry, room, humid, and wet conditions, respectively. The circles and diamonds indicate AE activities obtained by AE sensor in the upper and lower forcing blocks, respectively.

4 Discussion

4.1 Comparison with previous studies

The humidity dependence of the frictional properties of a quartz gouge reported by Frye & Marone (2002, hereafter referred to as FM2002) is plotted in Figure 3. P_v of FM2002 was calculated by assuming that the temperature was 25°C. Although Dieterich & Conrad (1984) stated that the friction coefficient was higher under drier conditions, FM2002 found that it did not depend on the humidity. The observations in this study are consistent with those of FM2002.

FM2002 modeled the frictional response against the sliding-rate steps using the RSF law with one state variable and different evolution law from Equation (3). These differences do not affect the estimation of a and the dependencies of a on P_v in FM2002, and the results of this study are similar. The humidity dependence of the evolution effect b in FM2002 was more consistent with that of b_2 than with that of b_1, suggesting that b in FM2002 corresponds to b_2 in this study. The critical slip distance Dc in FM2002 was several tens to hundred μm, while Dc_2 in this study was 20–30 μm. This discrepancy may have been caused by differences in the evolution law and gouge thickness (3 mm in FM2002 and 1–2 mm in the present study). However, the tendency that Dc takes a minimum at ~10 hPa is common. While a negative dependence of $a - b$ on P_v is common in FM2002 and this study, their magnitudes systematically differ, probably owing to differences in the sliding distances (Mair & Marone, 1999). The sliding distance was 5–9 mm in FM2002 and 50–100 mm in this study. Scuderi et al. (2014) found that

the friction drop associated with the stick-slip of a glass bead layer increased with increasing humidity. This is consistent with the negative P_v dependence of $a - b$ observed in this study.

4.2 Two state variables

The average diameter of gouge particles estimated from the particle size distribution (Figure S9 of Supporting Information) is ~25 μm and comparable to Dc_2. Because normal stress at a real area of contact junction is ~1 GPa (Dieterich & Kilgore, 1994; Teufel & Logan, 1977), a typical size of contact junction should be 2–3 μm and comparable to Dc_1. Therefore, the state variable θ_1 that evolves over Dc_1 may represent the average lifetime of the contact junction and b_1 is the average healing rate of the contact junction. Conversely, the state variable θ_2 would relate to the reorganization of gouge particles (FM2002) such as renewal of stress chains and Dc_2 may reflect the diffuseness of gouge particle networks or thickness of stress chains.

4.3 Implications for microscopic processes of friction

When contact junction growth occurs by the pressure solution (Scuderi et al., 2014; Yasuhara et al., 2005), the growth rate is controlled by the product of the water film thickness on the gouge particle surface and diffusivity of the solution along the contact junction if the pores in the gouge layer are empty (Gundersen et al., 2002). The water film thickens under higher humidity (Whalen, 1961). Because the diffusivity is proportional to the pressure gradient along the contact junction, the solution diffuses faster along a smaller contact junction (Weyl, 1959). Therefore, a contact junction with larger P_v/R_a, where R_a is the radius of the contact junction, increases faster. Consequently, the average size of the contact junction increased with increasing humidity, resulting in a negative P_v dependence of the *m*-value which is inversely proportional to the average AE size. When the pores are filled with liquid water, the solution diffuses into the pore water. Because more solution is transported along a smaller contact junction, this effect may be more significant for smaller contact junction. Consequently, the average AE size decreased (*m*-value increased) under wet conditions.

Figure 5a shows the relationship between normalized direct effect a/μ_i and α. The average of two tests under the same conditions was plotted. The relationships for room, humid, and wet conditions were concentrated around (a/μ_i, α) = (0.0086, 0.14) and that for dry condition was distinct at (0.011, 0.29). Frye & Marone (2002) and Scuderi et al. (2014) pointed out that the threshold humidity above which the gouge particle surface is completely covered by the water

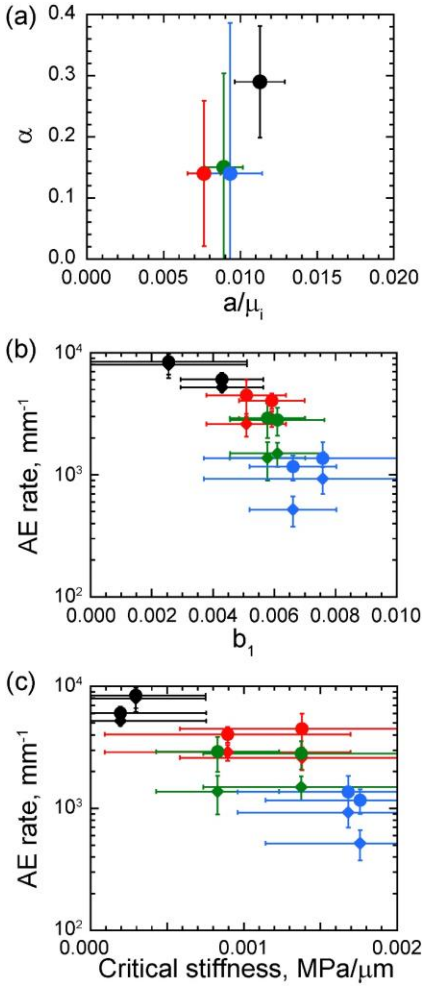

Figure 5. Relationships between parameters of RFS law and AE activity. (**a**) Normalized direct rate-dependence of friction a/μ_i vs. sliding-rate dependence of AE rate α. (**b**) Evolution parameter b_1 vs. AE rate. (**c**) Critical stiffness of gouge layer vs. AE rate.

film is 35-50% RH. RH and temperature of two tests under room conditions in this study were (35%, 16℃) and (45%, 14℃). Therefore, the gouge particle surface under dry conditions was only partially covered by the water film, whereas that under the other conditions was completely covered. The bipolarized relationship between a/μ_i and α likely reflects their sensitivity to the areal fraction of the water film on the surface of gouge particles.

Because b_1 represents the healing rate of the contact junction, the significant correlation between b_1 and the AE rate in Figure 5b indicates that AE activity is induced mainly by the failure of contact junctions (Bolton et al., 2022). Because healing is implemented by plastic deformation of the contact junction, b_1 represents the plasticity of the contact junction. By contrast, because AE events are generated by the brittle failure of the contact junctions, the AE rate reflects the brittleness of the contact junction. Therefore, the significant correlation shown in Figure 5b indicates that P_v controls the trade-off between the plasticity and brittleness of the contact junction.

The instability of the gouge layer is evaluated by the critical stiffness $k_c = \sigma_n(b-a)/Dc$ (Ruina, 1983). Figure 5c shows the relationship between the critical stiffness and AE rate. A longer critical slip distance Dc_2 was adopted as Dc to calculate k_c. With increasing P_v, the critical stiffness increases, and the AE rate decreases, indicating that the instabilities at the macroscopic and microscopic scales are affected by the presence of water in opposite manners. The underlying process of this apparent contradiction is the trade-off between the plasticity and brittleness of the contact junction, as shown in Figure 5b.

5 Summary

To understand underlying processes of friction of granular materials, we conducted sliding-rate step tests on a quartz gouge layer under various humidities using a rotary shear apparatus. We also monitored AE activity during sliding. We modeled frictional response using the RSF laws with two state variables. The one with the shorter critical slip distance represents the average lifetime of the contact junction. The other state variable corresponds to the average lifetime of the stress chains.

The *m*-value of AE activity decreased slightly with increasing water vapor. When the pores in the gouge layer were filled with water (wet conditions), the *m*-value increased. These humidity dependences of *m*-value suggest contact junction healing is likely achieved by the pressure solution.

The relationship between direct effect (a of RSF law) and rate-dependence of AE rate ($\alpha = d\ln N/d\ln V$) under dry conditions (5% RH) was distinct from those under other conditions (room, humid, and wet). This suggests these parameters are sensitive to the areal fraction of the water film on the gouge particle surface. A rise in humidity enhanced the contact junction healing, and the AE rate decreased, implying humidity controls the trade-off between the instability of the gouge layer and brittleness of the contact junction.

The underlying processes of friction were investigated from the contact junction healing standpoint. We demonstrated the ability of AE monitoring to provide insights into the micromechanics of friction from the perspective of the failure processes of contact junctions.

Understanding the micromechanics of friction can be deepened by studying AE activity during frictional sliding under more comprehensive conditions.

Acknowledgments

This study was supported by the Ministry of Education, Culture, Sports, Science and Technology (MEXT) of Japan, under its The Second Earthquake and Volcano Hazards Observation and Research Program (Earthquake and Volcano Hazard Reduction Research).

Open Research

The data used in this paper are available at (Yabe, 2023).

References

Asada, T., Suzuki, Z., & Tomoda, Y. (1951). Notes on the energy and frequency of earthquakes. *Bulletin of Earthquake Research Institute, 29*, 289-293.

Bedford, J. D., & Faulkner, D. R. (2021). The role of grain size and effective normal stress on localization and the frictional stability of simulated quartz gouge. *Geophysical Research Letters, 48*, e2020GL092023. https://doi.org/10.1029/2020GL092023

Bolton, D. C., Shreedharan, S., McLaskey, G. C., Rivière, J., Shokouhi, P., Trugman, D. T., & Marone, C. (2022). The high-frequency signature of slow and fast laboratory earthquakes. *Journal of Geophysical Research: Solid Earth, 127*, e2022JB024170. https://doi.org/10.1029/2022JB024170

Bolton, D. C., Shreedharan, S., Rivière, J., & Marone, C. (2020). Acoustic energy release during the laboratory seismic cycle: Insights on laboratory earthquake precursors and prediction. *Journal ofGeophysical Research: Solid Earth, 125*, e2019JB018975. https://doi.org/10.1029/2019JB018975

Bolton, D. C., Shreedharan, S., Rivière, J., & Marone, C. (2021). Frequency-magnitude statistics of laboratory foreshocks vary with shear velocity, fault slip rate, and shear stress. *Journal of Geophysical Research: Solid Earth, 126*, e2021JB022175. https://doi.org/10.1029/2021JB022175

Casas, N., Mollon, G., & Daouadji, A. (2023). Influence of grain-scale properties on localization patterns and slip weakening within dense granular fault gouges. *Journal of Geophysical Research: Solid Earth, 128*, e2022JB025666. https://doi.org/10.1029/2022JB025666

Chester, F. M., Evans, J. P., & Biegel, R. L. (2012). Internal structure and weakening mechanisms of the San Andreas Fault. *Journal of Geophysical Research: Solid Earth, 98*, 771-786. https://doi.org/10.1029/92jb01866

Dieterich, J. (1979). Modeling of rock friction 1. Experimental results and constitutive equations. *Journal of Geophysical Research, 84*, 2161-2168. https://doi.org/10.1029/JB084iB05p02161

Dieterich, J., & Conrad, G. (1984), Effect of humidity on time- and velocity dependent friction in rocks, *Journal of Geophysical Research, 89*, 4196-4202. https://doi.org/10.1029/JB089iB06p04196

Dieterich, J. H., & Kilgore, B. (1994), Direct observation of frictional contacts: New insights for state-dependent properties, *Pure and Applied Geophysics, 143*, 283–302. doi:10.1007/BF00874332

Frye, K., & Marone, C. (2002), Effect of humidity on granular friction at room temperature, *Journal of Geophysical Research: Solid Earth, 107*, ETG-11. https://doi.org/10.1029/2001jb000654

Gao, K., Guyer, R., Rougier, E., Ren, C. X., & Johnson, P. A. (2019). From stress chains to acoustic emission. *Physical Review Letters, 123*, 048003. https://doi.org/10.1103/PhysRevLett.123.048003

Gundersen, E., Renard, F., Dysthe, D. K., Bjørlykke, K., & Jamtveit, B. (2002). Coupling between pressure solution creep and diffusive mass transport in porous rocks. *Journal of Geophysical Research, 107*, 2317. https://doi.org/10.1029/2001JB000287

Ishimoto, M., & Iida, K. (1939), Observations sur les seisms energistréper le microseismograph construite dernierment (I), in Japanese, *Bulletin of Earthquake Research Institute, 17*, 443–478.

Johnson, P. A., Ferdowsi, B., Kaproth, B. M., Scuderi, M., Griffa, M., Carmeliet, J., Guyer, R. A., Le Bas, P-Y., Trugman, D. T., & Marone, C. (2013). Acoustic emission and microslip precursors to stick-slip failure in sheared granular material. *Geophysical Research Letters*, *40*, 5627-5631. https://doi.org/10.1002/2013gl057848

Johnson, D. H., Vahedifard, F., & Peters, J. F. (2021). Macroscale friction of granular soils under monotonic and cyclic loading based upon micromechanical determination of dissipated energy. *Acta Geotechnica*, *16*, 3027-3039. https://doi.org/10.1007/s11440-021-01224-7

Mair, K., Frye K. M., & Marone, C. (2002). Influence of grain characteristics on the friction of granular shear zones. *Journal of Geophysical Research: Solid Earth*, *107*, ECV 4-1-ECV 4-9. https://doi.org/10.1029/2001jb000516

Mair, K. & Marone, C (1999), Friction of simulated fault gouge for a wide range of velocities and normal stresses, *Journal of Geophysical Research: Solid Earth*, *104*, 28899-28914. https://doi.org/10.1029/1999jb900279

Marone, C., Hobbs, B. E., & Ord, A. (1992). Coulomb constitutive laws for friction: Contrasts in frictional behavior for distributed and localized shear. *Pure and Applied Geophysics*, *139*, 195-214. https://doi.org/10.1007/bf00876327

Marone, C. & Scholz, C. H. (1989). Particle-Size Distribution and Microstructures within Simulated Fault Gouge. *Journal of Structural Geology*, *11*, 799-814. https://doi.org/10.1016/0191-8141(89)90099-0

Mngadi, S. B., Tsutsumi, T., Onoe, Y., Manzi, M. S. D., Durrheim, R. J., Yabe, Y., Ogasawara, H., Kaneki, S., Wechsler, N., Ward, A. K., Naoi, M., Moriya, H., Nakateni, M., & the DSeis team (2021). The effect of a gouge layer on rupture propagation along brittle shear fractures in deep and high-stress mines. *International Journal of Rock Mechanics and Mining Sciences*, *137*, 104454. https://doi.org/10.1016/j.ijrmms.2020.104454

Moore, D. E., Lockner, D. A., Ito, H., Ikeda, R., Tanaka, H., & Omura, K. (2009). Geometry of the Nojima fault at Nojima-Hirabayashi, Japan – II. Microstructures and their implications for permeability and strength. *Pure and Applied Geophysics*, *166*, 1669-1691. https://doi.org/10.1007/s00024-009-0513-2

Nakatani, M. & Scholz, C. (2004). Frictional healing of quartz gouge under hydrothermal conditions: 1. Experimental evidence for solution transfer healing mechanism. *Journal of Geophysical Research: Solid Earth*, *109*, B07201. https://doi.org/10.1029/2001jb001522

Niemeijer, A. R., Spiers, C. J., & Peach, C. J. (2008). Frictional behaviour of simulated quartz fault gouges under hydrothermal conditions: Results from ultra-high strain rotary shear experiments. *Tectonophysics*, *460*, 288-303. https://doi.org/10.1016/j.tecto.2008.09.003

Ostapchuk, A., Morozava, K., Markov, V., Pavlov, D., & Popov, M. (2021). Acoustic Emission Reveals Multiple Slip Modes on a Frictional Fault. *Frontiers in Earth Science*, *9*, 657487. https://doi.org/10.3389/feart.2021.657487

Rice, J. (1993). Spatio-temporal complexity of slip on a fault. *Journal of Geophysical Research*, *98*, 9885-9907. https://doi.org/10.1029/93JB00191

Rouet-Leduc, B., Hulbert, C., Bolton, D. C., Ren, C. X., Riviere, J., Marone, C., Guyer, R. A., & Johnson, P. A. (2018). Estimating fault friction from seismic signals in the laboratory. *Geophysical Research Letters*, *45*, 1321–1329. https://doi.org/10.1002/2017GL076708

Ruina, A. (1983). Slip instability and state variable friction laws. *Journal of Geophysical Research*, *88*, 10359-10370. https://doi.org/10.1029/JB088iB12p10359

Scuderi, M. M., Capenter, B. M., & Marone, C. (2014). Physicochemical processes of frictional healing: Effects of water on stick-slip stress drop and friction of granular fault gouge.

Journal of Geophysical Research: Solid Earth, *119*, 4090-4105. https://doi.org/10.1002/2013jb010641

Tetens, O. (1930). Über einige meteorologische Begriffe. Z. Geophys 6: 297-309.

Teufel, L. W., & Logan, J. M. (1977), Effect of displacement rate on the real area of contact and temperatures generated during frictional sliding of Tennessee sandstone, *Pure and Applied Geophysics*, *116*, 840–865. https://doi.org/10.1007/BF00876541

Weyl, P. K. (1959). Pressure solution and the force of crystallization: a phenomenological theory. *Journal of Geophysical Research*, *64*, 2001-2025. https://doi.org/10.1029/JZ064i011p02001

Whalen, J. W. (1961). Thermodynamic Properties of Water Adsorbed on Quartz. *The Journal of Physical Chemistry*, *65*, 1676-1681. https://doi.org/10.1021/j100827a003

Yabe, Y. (2023). Humidity dependence of parameters of RSF law and AE activity [Dataset]. Zenodo. https://doi.org/10.5281/zenodo.10081007

Yabe, Y. (2002), Rate dependence of AE activity during frictional sliding, *Geophysical Research Letters*, *29*, 26. https://doi.org/10.1029/2001GL014369

Yasuhara, H., Marone, C., & Elsworth, D. (2005), Fault zone restrengthening and frictional healing: The role of pressure solution, *Journal of Geophysical Research: Solid Earth*, *110*, B06310. doi:10.1029/2004JB003327